Utilisation of spatial derivative measurements in circular diffuse optical tomographic imaging to improve image resolution and contrast

D. Lighter, S. Jiang, H. Dehghani

Abstract. **The resolution of images recovered using diffuse optical tomography without spatial prior information is inherently limited due to the diffusive nature of light transport in scattering dominated biological tissue. Several studies have previously reported an improvement in depth sensitivity in near infrared spectroscopy by considering the subtraction of two neighbouring measurements. A nearest neighbour, spatial derivative based algorithm is presented, in which the difference between neighbouring source-sharing source–detector pairs is considered for tomographic reconstruction. Using a circular, inward-facing optode geometry, it is shown that deeper abnormalities in oxyhaemoglobin, deoxyhaemoglobin and water can be recovered with better localisation and contrast as compared to reconstructing using absolute values of multi-wavelength data. Relative improvements of up to 25 % in quantitative accuracy of recovered physiological values are demonstrated at better resolution for cancerous tissue in a heterogeneous breast model, when using this proposed spatial derivative based parameter reconstruction.**

Keywords: diffuse optical tomography, spatial derivative, circular geometries.

1. Introduction

Diffuse optical tomography (DOT) is a non-invasive, high contrast and low-cost imaging technique capable of recovering the underlying spatial distribution of optical properties within biological tissue. Near infrared (NIR) light (650 – 930 nm) is injected into the tissue and subsequently measured at multiple tissue boundary locations, thus allowing tomographic reconstruction. The use of multispectral measurements at two or more wavelengths permits the spectral decoupling of chromophore contributions to attenuation, to enable recovery of underlying concentrations, such as oxyhaemoglobin (HbO), deoxyhaemoglobin (Hb) and water (H_2O), which can provide clinically relevant information about the pathophysiological state of diseased tissue. When recovering absolute values using conventional (CONV) DOT, the inverse problem is solved by minimising the difference between the measured data and modelled (forward)

data in a least squares sense, over multiple measurements. This is typically achieved using nonlinear iterative reconstruction schemes involving either; optimisation schemes where the gradient of the objective function is calculated directly [1, 2], or Newton-like approaches implemented in a Levenberg–Marquardt procedure [3, 4].

Several alternative reconstruction algorithms have been previously proposed based on fitting to the first order derivative of the boundary data, with respect to either a difference in wavelength or a difference in optodes spatial location. For multiwavelength DOT, a spectral derivative approach [5 – 7], which considers the difference in boundary data between multiple wavelength pairs, has demonstrated an inherent insensitivity to source or detector coupling offsets and a reduction in errors resulting from inaccurate geometric modelling. Spatial derivative algorithms have been proposed that demonstrate improvements in depth sensitivity in reflectance imaging geometries. One example is spatially resolved spectroscopy (SRS) [8], a commonly used near-infrared spectroscopy (NIRS) technique implemented in commercially available devices (NIRO200NX, Hamamatsu Photonics, Shizuoka, Japan), in which the total oxygen index is calculated from the slope of light attenuation versus source–detector separation using an analytical solution for a homogeneous, semi-infinite medium. It has been widely argued that the SRS method provides greater sensitivity to changes at deeper layers compared to when considering absolute continuous wave (CW) measurements, resulting in an improved accuracy of recovered cerebral oxygenation [9]. For a subtraction-based approach in time-resolved (TR) NIRS, also considering a semi-infinite reflectance geometry, optical absorption (μ_a) was estimated by calculating the difference in variance and mean time of flight between the two nearby source-sharing source–detector pairs. This demonstrated an improvement in depth sensitivity compared to conventional NIRS measurements [10], attributed to the greater difference in time of flight at deeper layers than shallower layers, when the corresponding sensitivity profiles for two measurements are subtracted. More specifically, results revealed that the proposed subtraction-based approach provides a unique and selective sensitivity to a layer at a specific depth which was argued to be applicable to either CW or TR measurements. Applications of derivative based techniques for tomographic image reconstruction include (1) temporal difference imaging such as those used in functional-NIRS [11], (2) the use of relative intensities for DOT and bioluminescence tomography [12], which has been demonstrated to enable calibration for the unknown optical properties in a mouse model, and (3) a proposed geometric-sensitivity-difference based algo-

D. Lighter, H. Dehghani University of Birmingham, Sci-Phy-4-Health Centre for Doctoral Training, Edgbaston, Birmingham, UK, B15 2TT; e-mail: dml413@student.bham.ac.uk, h.dehghani@cs.bham.ac.uk;
S. Jiang Dartmouth College, Thayer School of Engineering, Hanover, USA, NH 03755; e-mail: Shudong.Jiang@dartmouth.edu

rithm for DOT [13], in which the subtraction of a combination of source-sharing source–detector pairs reported improvements in object depth-localisation and optical properties estimation using both simulated and experimental data for an outward-facing, circular geometry, such as those used for endoscopic imaging.

Circular, in-ward facing optode arrangements are commonly implemented geometries for data acquisition in DOT systems, with applications including breast imaging for cancer detection [14] and finger imaging for arthritis diagnostics and monitoring [15]. In these applications, accurate localisation and quantitative values are crucial to enable characterisation of diseased tissue, often located deep within the anatomy, creating a need for algorithms that can improve resolution and accuracy of recovered chromophore maps at deeper regions within the centre of these circular geometries. Motivated by the discussed studies reporting the benefits of spatial derivative boundary measurements on depth sensitivity, in this work a nearest neighbour, spatial derivative (NNSD) DOT algorithm is presented, in which the subtraction between neighbouring source-sharing source–detector pairs is considered for tomographic reconstruction. The performance of NNSD-DOT is evaluated in comparison to CONV-DOT, where only the absolute values of the boundary data are considered, for circular inward-facing optode geometries using both simulated and experimental data.

2. NNSD algorithm theory and derivation

In CONV-DOT, absolute values are recovered by minimising the difference between the measured data, ϕ^m, and forward data, ϕ^f, in a least squares sense over a number of sources (N_s) and detectors (N_d), with the objective function defined as follows:

$$\chi^2 = \sum_{i=1}^{N_s} \sum_{j=1}^{N_d} (\phi_{ij}^m - \phi_{ij}^f)^2. \tag{1}$$

A NNSD-DOT algorithm is described here, where an alternative objective function is considered, based on the spatial derivative of neighbouring boundary measurements for each given source. Motivation for this choice of the objective function was to build upon previously reported improvements in depth resolution demonstrated when using single source-sharing source–detector pairs with NIRS data, to be extended to tomographic reconstruction. In the proposed NNSD-DOT algorithm the difference between the measured relative data from two neighbouring source-sharing source–detector pairs and the corresponding model for the same pair is instead minimised:

$$\tilde{\chi}^2 = \sum_{i=1}^{N_s} \sum_{j=1}^{N_d} (\tilde{\phi}_{ij}^m - \tilde{\phi}_{ij}^f)^2, \tag{2}$$

where $\tilde{\phi}_{ij} = \phi_{ij} - \phi_{ij+1}$.

By considering the first two terms of the Taylor's expansion of $\mathrm{d}\tilde{\chi}^2/\mathrm{d}\mu$ around μ (where μ is the absorption coefficient, reduced scattering coefficient or both) for some close initial guess μ_0, typically obtained from a homogeneous fitting algorithm [16]:

$$\frac{\mathrm{d}\tilde{\chi}^2}{\mathrm{d}\mu} = \frac{\mathrm{d}\tilde{\chi}^2}{\mathrm{d}\mu}(\mu_0) + (\mu - \mu_0)\frac{\mathrm{d}^2\tilde{\chi}^2}{\mathrm{d}\mu^2} + \dots. \tag{3}$$

The update equation at the kth iteration can be obtained, as follows:

$$\Delta\mu = \mu_{k+1} - \mu_k = \left(\frac{\mathrm{d}^2\tilde{\chi}^2}{\mathrm{d}\mu^2}(\mu_k)\right)^{-1}\frac{\mathrm{d}\tilde{\chi}^2}{\mathrm{d}\mu}(\mu_k). \tag{4}$$

The first and second derivatives of $\tilde{\chi}^2$ with respect to μ can then be calculated from Eqn (2), giving:

$$\frac{\mathrm{d}\tilde{\chi}^2}{\mathrm{d}\mu} = -2\frac{\mathrm{d}\tilde{\phi}^f}{\mathrm{d}\mu}(\tilde{\phi}^m - \tilde{\phi}^f); \tag{5}$$

and

$$\frac{\mathrm{d}^2\tilde{\chi}^2}{\mathrm{d}\mu^2} = -2\left(\frac{\mathrm{d}^2\tilde{\phi}^f}{\mathrm{d}\mu^2}(\tilde{\phi}^m - \tilde{\phi}^f) - \frac{\mathrm{d}\tilde{\phi}^f}{\mathrm{d}\mu}\frac{\mathrm{d}\tilde{\phi}^f}{\mathrm{d}\mu}\right). \tag{6}$$

In CONV-DOT typically only the first order derivative of the measurement quantities with respect to optical properties are considered, with the second derivative assumed to be negligible. Following from this, it is also assumed here that $\mathrm{d}^2\tilde{\phi}^f/\mathrm{d}\mu^2$ can be ignored. Substituting these derivatives into Eqn (4) results in the Moore–Penrose update equation,

$$\Delta\mu = (\tilde{J}^T\tilde{J} + \tau I)^{-1}\tilde{J}^T\Delta\tilde{\phi}, \tag{7}$$

where the NNSD-Jacobian is defined as

$$\tilde{J} = \frac{\mathrm{d}\tilde{\phi}^f}{\mathrm{d}\mu}$$

and the NNSD-data difference becomes $\Delta\tilde{\phi} = \tilde{\phi}^m - \tilde{\phi}^f$. As is commonly implemented when solving ill-posed inverse problems, Tikhonov regularisation has been included in Eqn (7) to dampen very small singular values and stabilise convergence [17], with a regularisation parameter. As CW measurements were considered in this work, where changes in absorption are recovered and only the amplitude of light was considered, the time independent diffusion approximation to the radiative transport equation was used as a forward model for photon transport in biological tissue,

$$-\nabla \cdot [D\nabla\phi(r)] + \mu_a\phi(r) = S_0(r), \tag{8}$$

where $D(r) = \{3[\mu_a(r) + \mu_s(r)]\}^{-1}$ is the diffusion coefficient, r is the coordinate, $S_0(r)$ is the isotropic source, and $\phi(r)$ is the photon fluence rate for a given wavelength λ. This relies on the assumptions that reduced scattering dominates over absorption ($\mu_s' \gg \mu_a$) and that fluence is isotropic after a single scattering transport length. In this work multiwavelength data were considered, enabling the recovery of functional parameters, StO$_2$ (oxygen saturation), tHb (total haemoglobin) and H$_2$O from the wavelength dependent absorption coefficient, with a spectrally constrained DOT algorithm, in which the chromophore extinction coefficients were incorporated into the Jacobian matrix, thus allowing direct update of concentration values at each iteration in a single step using measurements at all wavelengths simultaneously, as this approach has been shown to improve accuracy in reconstructed images when using multispectral data [18, 19]. The scatter amplitude (S_a) and scatter power (S_p) parameters, which reflect particle scattering centre size and scatterer number density respectively according to Mie theory [20], were

not recovered and set as homogeneous *a priori* constants throughout this work; however, it is straightforward to extend the derivation of the NNSD algorithm to include phase in frequency domain data if desired, to facilitate the recovery of both absorption and scattering properties. An index-mismatched type III condition, commonly known as the Robin boundary condition, was used to represent the tissue–air boundary. To solve the forward model numerically, finite element method (FEM) meshes were created over which the problem was discretised, and a more sparse, regular mesh was used as a basis when solving the inverse problem. All image recovery algorithms were implemented using FEM package NIRFAST [4]. In practice, calculation of $\tilde{J}$ and $\Delta\tilde{\phi}$ was implemented by computing J and $\Delta\phi$ in the conventional manner for each source/detector pair, identical to the formalism utilised in CONV-DOT, and subtracting the difference data or rows of J for the corresponding measurements, shown in Eqn (9) for the ith source over j number of measurements. All computations were implemented in matrix notation, which was most computationally efficient for MATLAB R2017a (Mathworks, Natick, USA):

$$\Delta\tilde{\phi} = \begin{pmatrix} \phi^{m}_{s_i d_1} - \phi^{f}_{s_i d_1} \\ \vdots \\ \phi^{m}_{s_i d_{j-1}} - \phi^{f}_{s_i d_{j-1}} \end{pmatrix} - \begin{pmatrix} \phi^{m}_{s_i d_2} - \phi^{f}_{s_i d_2} \\ \vdots \\ \phi^{m}_{s_i d_j} - \phi^{f}_{s_i d_j} \end{pmatrix}, \tag{9a}$$

$$\tilde{J} = \begin{pmatrix} J_{s_i d_1} \\ \vdots \\ J_{s_i d_{j-1}} \end{pmatrix} - \begin{pmatrix} J_{s_i d_2} \\ \vdots \\ J_{s_i d_j} \end{pmatrix}. \tag{9b}$$

3. Simulation methods and results

3.1. Quantitative metrics

To measure the quantitative accuracy of the recovered images, three metrics were used in this work: recovered contrast (RC), the area ratio (AR) and the mean square error (MSE). RC is the recovered contrast between the ground truth of the anomaly region and the ground truth of the background region, defined as follows:

$$\text{RC}^j = \frac{1}{N_{\text{an}}} \sum_{i=1}^{N_{\text{an}}} c_i^j \left(\frac{1}{N_{\text{b}}} \sum_{i=1}^{N_{\text{b}}} \tilde{c}_i^j \right)^{-1}, \tag{10}$$

where N_{an} is the number of nodes in the ground truth anomaly region, N_{b} is the number of background nodes outside the ground truth anomaly region, c_i^j is the chromophore concentration of the nodes inside the ground truth anomaly region, $\tilde{c}_i^j$ is the chromophore concentration of the nodes in the ground truth background region, i is the node index and j is the corresponding chromophore (HbO, Hb, and H$_2$O). An optimum value for RC is equal to the contrast ratio of the value of the anomaly region over the value of the background region in the ground truth. AR is the ratio of the area of the recovered anomaly and the ground truth target area, providing a measure of the accuracy of the recovered target size:

$$\text{AR} = \frac{|\text{ROI}|}{|\text{tROI}|}, \tag{11}$$

where ROI is the area where $c > \gamma \max(c)$, tROI is the ground truth anomaly region, and γ is a predefined threshold chosen to be 0.65 based on visual inspection of images that consistently separated the anomaly from the background. Lower AR values correspond to a better resolved anomaly. Finally, the mean square error between the ground truth and recovered values was calculated as

$$\text{MSE} = \frac{1}{N} \sum_{j=1}^{N} (c_i^j - \tilde{c}_i^j)^2, \tag{12}$$

where N is the total number of nodes, c_i^j is the recovered concentration and $\tilde{c}_i^j$ is the ground truth concentration. A lower value for MSE indicates less difference between the ground truth and the recovered image across the whole domain. Statistical analysis when comparing the two methods, CONV-DOT against NNSD-DOT, with simulated noise were carried out using a paired sample T-test, with the null hypothesis that the means of both algorithms are the same and a threshold of p less than 0.05 being taken as significant.

3.2. Multiple anomaly model

Simulated data for a simple 2D circular geometry were first considered. A 43 mm radius circle was discretised into an FEM mesh composed of 1785 nodes and 3418 linear triangular elements, used as a basis for the forward problem, while a regular grid of 648 nodes and 1230 linear triangular elements was used as a basis for the inverse problem. Sixteen co-located sources and detectors were placed equidistantly along the circle boundary, corresponding to the system optode fibres, except with the source positions located a single scattering transport length within the boundary, as shown in Fig. 1. Simulated CW data were generated at 13 wavelengths (700, 720, 740, 750, 765, 780, 790, 800, 820, 840, 860, 880 and 900 nm). These dimensions and wavelengths were chosen to match the specifications of the imaging system used to provide experimental data in Section 5. Each source was illuminated individually, whilst the remaining 15 optodes were used as detectors, resulting in 240 individual source–detector pair measurements per wavelength. The regularisation parameter, τ, was heuristically set throughout this work to an initial value of $10 \max(\tilde{J}^T \tilde{J})$ for both algorithms, and monotonically decreased at each iteration by a factor of $10^{0.25}$.

Background concentrations for HbO, Hb and H$_2$O were set to physiologically realistic values of 10 µMol, 10 µMol and 40%, respectively. Three circular anomaly regions of 7.5 mm radius were added simultaneously within the same model, each providing 2:1 contrast in either HbO, Hb or H$_2$O and separated by 120° around the centre, as shown in Fig. 1. S_{a} and S_{p} were assumed to be homogeneous and known at physiologically realistic values of 1.34 mm^{-1} and 0.56, respectively. The radial depths of these anomalies centres from the external boundary were varied at 11, 17, 23, 29 and 35 mm. To represent more experimentally realistic models, reconstructions were also carried out with 0.5% and 1% normally distributed random Gaussian noise added to the boundary data. All simulated experiments were repeated 10 times, to allow calculation of the mean and standard deviation for the quantitative evaluation metrics. Only images for 0% and 1% noise have been

Table 1. The values of p for the paired sample T-test assessing the difference between the means of CONV-DOT and NNSD-DOT, for all simulated depths for recovered HbO, Hb or H_2O, with either 0.5% or 1% added noise for all metrics.

Component	Depth/mm	RS		MSE		AR	
		0.5%	1%	0.5%	1%	0.5%	1%
HbO	11	0.56	0.32	0.027*	0.28	0.47	0.49
	17	0.027*	0.13	0.77	0.19	0.0020*	0.19
	23	0.020*	0.084	0.13	0.32	0.0039*	0.051
	29	0.037*	0.049*	0.19	0.084	0.0195*	0.0098*
	35	0.70	0.037*	0.92	0.70	0.65	0.049*
Hb	11	0.922	0.43	0.037*	0.0098*	0.70	0.25
	17	0.0059*	0.0039*	0.065	0.16	0.46	0.0039*
	23	0.0039*	0.0020*	0.0020*	0.0039*	0.0020*	0.0020*
	29	0.0059*	0.0098*	0.065	0.049*	0.0020*	0.018*
	35	1.0	0.0195*	0.63	0.13	0.86	0.037*
H_2O	11	0.38	0.63	0.0020*	0.13	0.035*	0.28
	17	0.19	0.38	0.28	0.32	0.025*	0.23
	23	0.0020*	0.23	0.49	0.020*	0.0078*	0.43
	29	0.014*	0.38	0.037*	0.43	0.0059*	0.70
	35	0.77	0.77	0.16	0.23	0.43	0.0039*

* Significant values using a paired sample T-test.
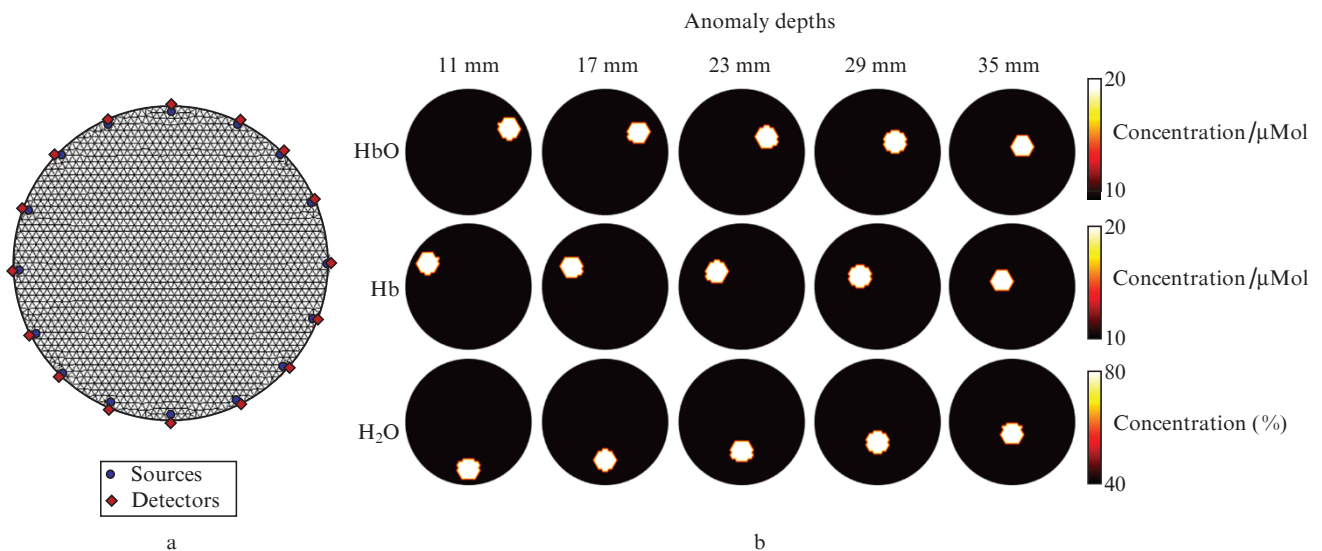
Figure 1. (a) Circular FEM mesh used as a basis for the forward model, and corresponding source and (b) detector positions of 3 anomalies providing 2:1 contrast in HbO, Hb and H_2O simulated at five depths.

shown; however, quantitative values for both noise profiles are displayed in Table 1.

In the case of 0% noise, when the abnormalities are close to the boundary at a depth of 11 mm, both algorithms performed similarly, with recovered images for all three chromophores appearing qualitatively similar and all three quantitative evaluation metrics recovering nearly identical values. As the reconstructed abnormalities moved deeper towards the circle centre, it can be clearly seen the NNSD-DOT algorithm consistently outperformed CONV-DOT in maintaining the quality of the reconstructed anomaly when no noise was added. This was again supported by all three
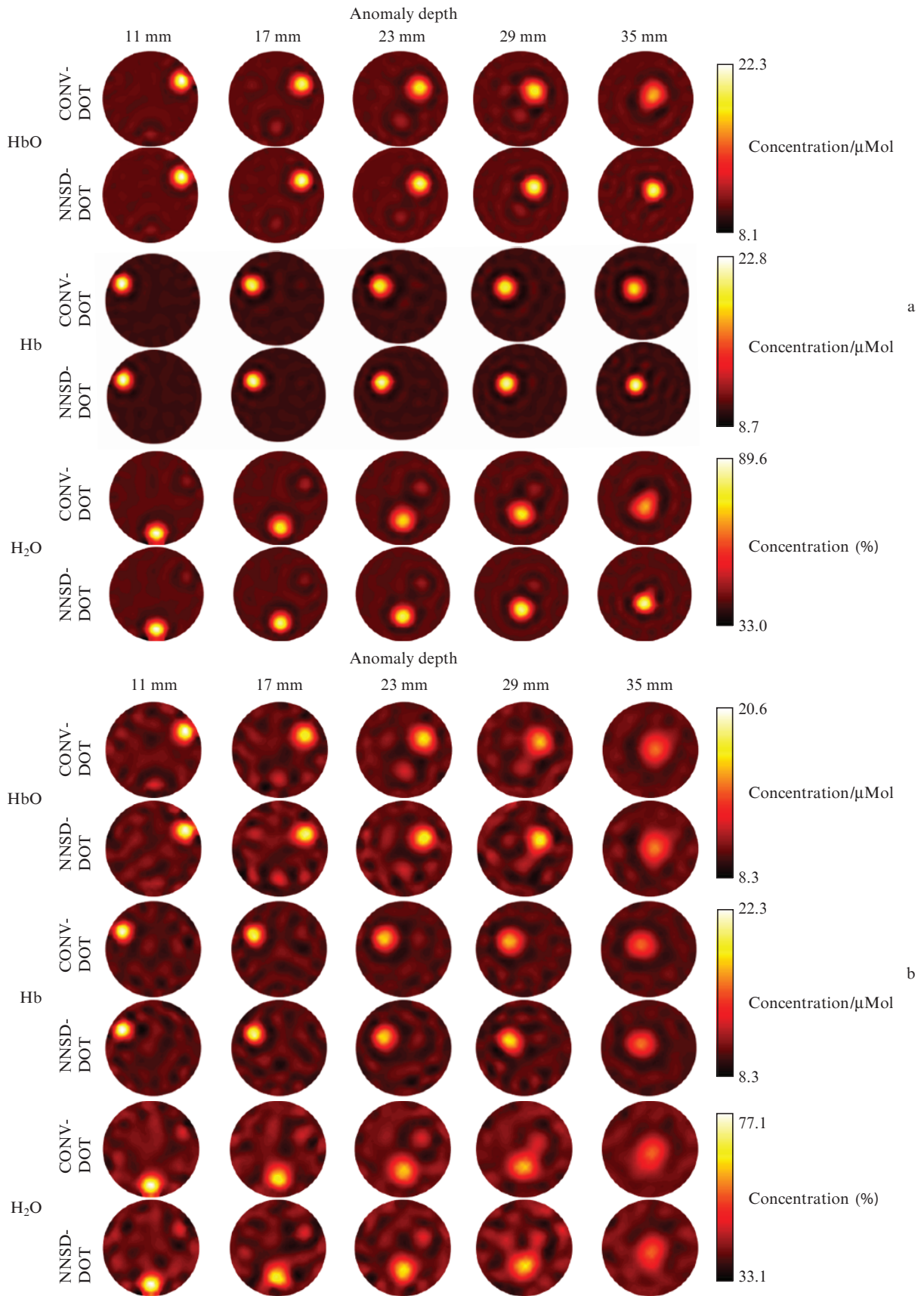
Figure 2. Reconstructions using both CONV-DOT and NNSD-DOT, for simulated data when three 2:1 contrast targets of HbO, Hb and H2O were simultaneously added at 120° separations. Results are shown for five depths (a) in the absence of Gaussian noise and (b) in the presence of 1% Gaussian noise.

quantitative evaluation metrics (Fig. 3). At depths of 17 mm to 35 mm, RC values were always closer to the target value of 2 for NNSD-DOT, indicating an improved contrast of the recovered anomaly against background, MSE values were consistently lower for NNSD-DOT, demonstrating that the recovered image was overall more similar to the ground truth and AR values were lower for NNSD-DOT, indicating a better resolved reconstructed abnormality.

In the presence of 0.5% and 1% Gaussian noise, the difference between the two algorithms was more complex. One can see from Fig. 3 that when the anomalies were close to the boundary at 11 mm depth, similar reconstructions were achieved by each algorithm, with similar qualitative appearance and no statistical difference between the two algorithms in RC or AR, with the exception of AR for H_2O with 0.5% noise. RC values were generally higher for the NNSD algorithm with added noise at depths of 17, 23, and 29 mm, with statically significant

differences for 0.5% noise for all these depths with the exception of H_2O at 17 mm.

For RC with 1% added noise, significance was achieved at 29 mm and 35 mm for HbO, although p-values were close to significance for 17 mm and 23 mm, and depths greater than or equal to 17 mm for Hb, but not for any H_2O reconstructions (see Table 1). AR values were also typically lower for NNSD-DOT at depths of 17 mm or more in both noise profiles, indicating the anomaly was better resolved, although statistical significance was only reached for certain chromophores at certain depths, again more often for 0.5% noise than 1%. In terms of MSE, in several cases the performance of NNSD-DOT was significantly inferior at shallow depths of 11 mm and 17 mm, and only minimal improvement was seen at depths greater than 23 mm in the presence of noise, although most of these results did not demonstrate any statistical significant difference between the two algorithms. These results indicate that in the presence of noise, although the abnormalities are generally better resolved and have improved contrast
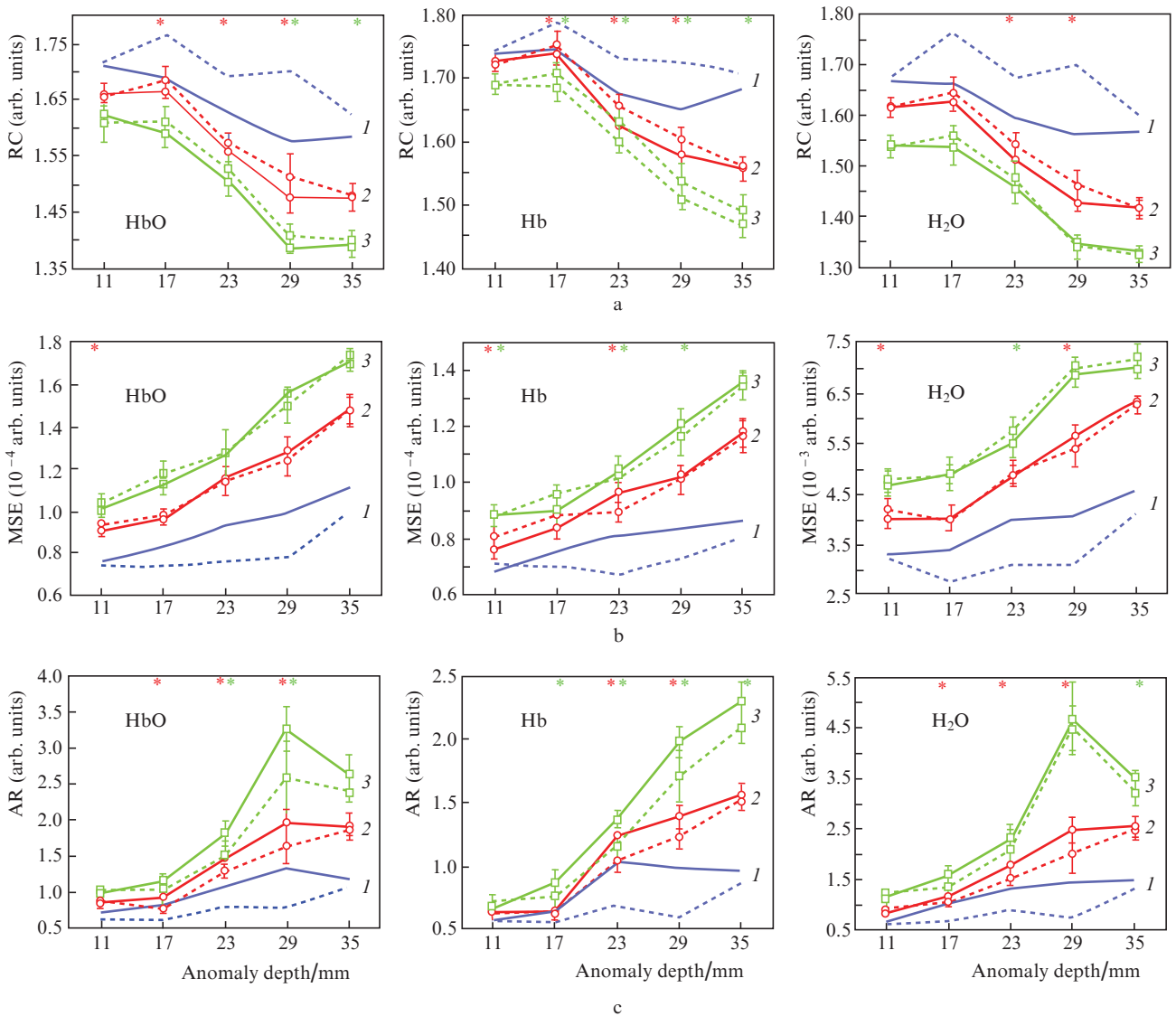
Figure 3. Plots against target anomaly depth: (a) recovered contrast of anomaly region compared to background; (b) mean square error and (c) area ratio of recovered anomaly to background, shown for all three chromophores with (*1*) 0%, (*2*) 0.5% and (*3*) 1% added Gaussian noise. Statistically significant differences between the two algorithms are highlights with * at the top, left of the tick for 0.5% and right of the tick for 1%.

using NNSD-DOT, the overall MSE is either significantly inferior if abnormalities are close to the boundary or there is often no significant difference if abnormalities are deeper when using NNSD-DOT, attributed to an increase in the number of image artefacts in the background.

3.3. Asymmetric heterogeneous model

An asymmetric, heterogeneous model designed to provide a basic representation of the human breast geometry was generated, to provide a more geometrically realistic example of biological tissue against which the algorithms performance could be evaluated. The model consisted of the same mesh geometry and simulation settings as in Section 3.2, but with a thin outer layer of adipose tissue and an asymmetrical inner layer of glandular tissue assigned. Expected physiological values for StO_2, tHb and H_2O for these regions were assigned respectively as 70%, 17 μMol and 71% in adipose tissue and 69%, 22 μMol and 70% in glandular tissue, based on values for the corresponding tissue type in the previous literature [21]. A circular anomaly region was added to represent a cancerous tumour, with a diameter of 15 mm and a centre at depth of 28 mm from the boundary, expected to be realistic quantitative changes occurring in a cancerous breast tumour of 40%, 40.0 μMol and 40% for StO_2, tHb and H_2O, respectively [22]. Due to the additional challenges of separating scattering and absorption in CW, S_a and S_p were assumed homogeneous,

in this case set to the values for adipose of 1.34 mm^{-1} and 0.56, respectively.

Reconstructed distributions of the parameters are shown in Fig. 4, along with corresponding line profiles along the horizontal diameter. A qualitative improvement is visible in the NNSD-DOT case with fewer image artefacts close to the optode locations on the boundary and improved contrast of the cancer for all three metabolic parameters. Mean values from Fig. 4 in the region defining the cancerous anomaly in the ground truth image, were more accurate in the NNSD-DOT case (48.0%, 34.0 μMol and 51%) than for CONV-DOT (46.5%, 34.9 μMol and 48.2%) for StO_2, tHb and H_2O respectively, corresponding to relative improvements of 19.4%, 14.9% and 25.2% closer to the ground truth. Table 2 shows the mean values of all three quantitative evaluation metrics, RC, MSE and AR, for 10 repeat experiments when either 0%, 0.5% or 1% Gaussian noise was added to the simulated data. In the absence of noise, all three metrics were significantly superior in the NNSD case, with RC values closer to the target values of 1.97, 0.574 and 0.569 for tHb, StO_2 and H_2O respectively, lower MSE, and lower AR indicating the cancer has been better resolved. When 0.5% noise was added, RC was significantly improved for tHb when using NNSD, MSE was significantly lower for all three physiological parameters for NNSD, attributed to the reduced number of image artefacts close to the optode locations, and AR was significantly lower for StO_2 and H_2O; however, with
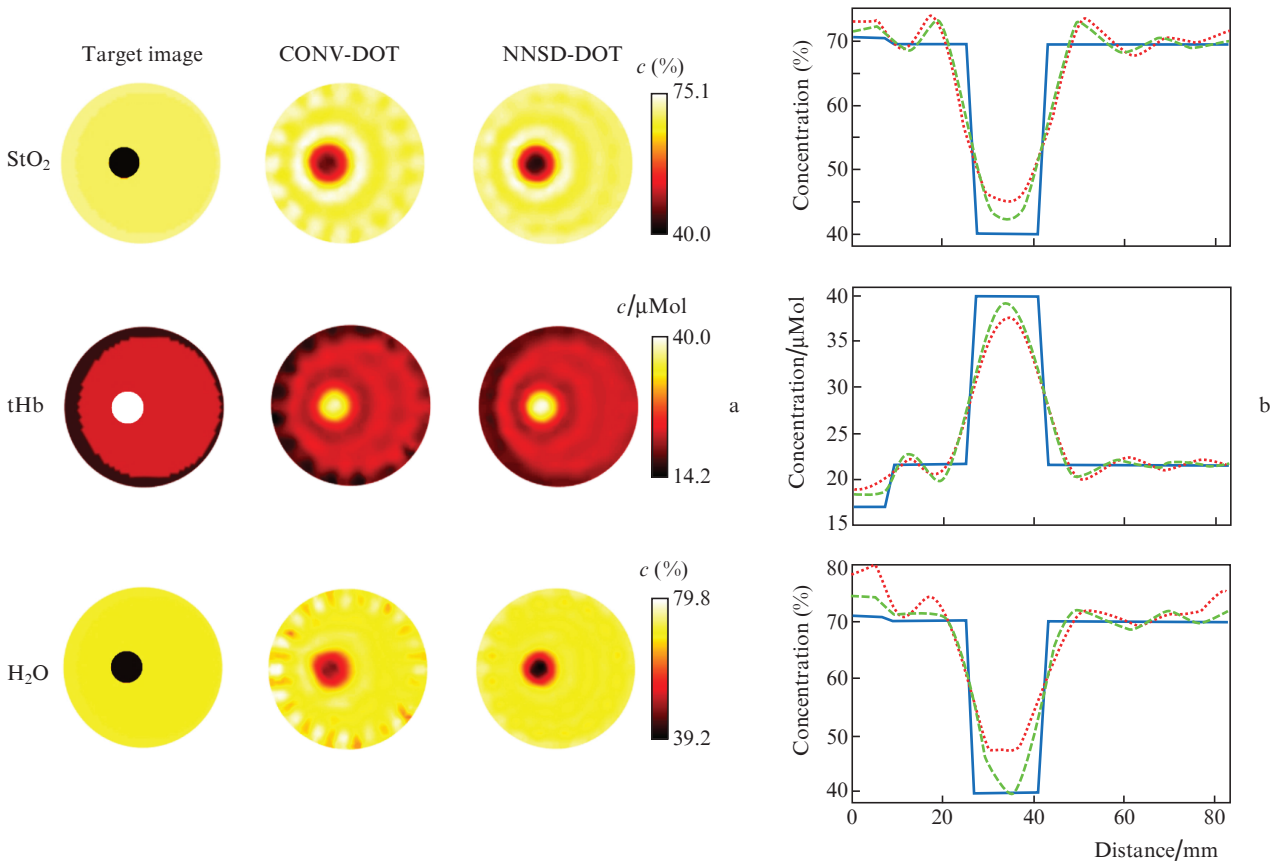
Figure 4. (a) Reconstructions for simulated asymmetric, heterogeneous breast model using both algorithms and (b) corresponding line profiles [(solid curves) for a target image; (dotted and dashed curves) for reconstructions obtained using CONV-DOT and NNSD-DOT, respectively] along the horizontal diameter; c is the concentration.

Table 2. Quantitative evaluation metrics, recovered using the NNSD-DOT and CONV-DOT algorithms for the heterogeneous model, either with 0%, 0.5% or 1% added Gaussian noise.

Functional parameter	Noise level (%)	RC		MSE		AR	
		NNSD-DOT	CONV-DOT	NNSD-DOT	CONV-DOT	NNSD-DOT	CONV-DOT
tHB	0	1.79	1.68*	2.41×10^{-6}	3.99×10^{-6}*	1.29	2.08*
	0.5	1.66	1.64*	3.71×10^{-6}	3.97×10^{-6}*	1.45	1.49
	1	1.55	1.56	4.48×10^{-6}	4.57×10^{-6}	1.93	2.02
StO$_2$	0	0.621	0.675*	5.64×10^{-4}	1.28×10^{-3}*	0.625	1.65*
	0.5	0.707	0.707	1.42×10^{-3}	1.69×10^{-3}*	0.775	1.18*
	1	0.743	0.748	1.48×10^{-3}	1.50×10^{-3}	0.125	0.221
H$_2$O	0	0.636	0.712*	8.92×10^{-4}	2.83×10^{-3}*	0.396	2.19*
	0.5	0.753	0.744	2.54×10^{-3}	3.67×10^{-3}*	1.23	2.51*
	1	0.813	0.820	2.98×10^{-3}	2.62×10^{-3}	0.396	2.26

* Significant values using a paired sample T-test.

1% added noise for the heterogeneous model there was no significant difference between the two algorithms in any cases, again indicating a greater impact of Gaussian noise on the NNSD algorithm.

3.4. Anomaly pair resolution model

To compare reconstruction resolution between CONV and NNSD, the 2D circular model presented in Section 3.2 was used, except with a pair of identical, 15 mm diameter anoma-
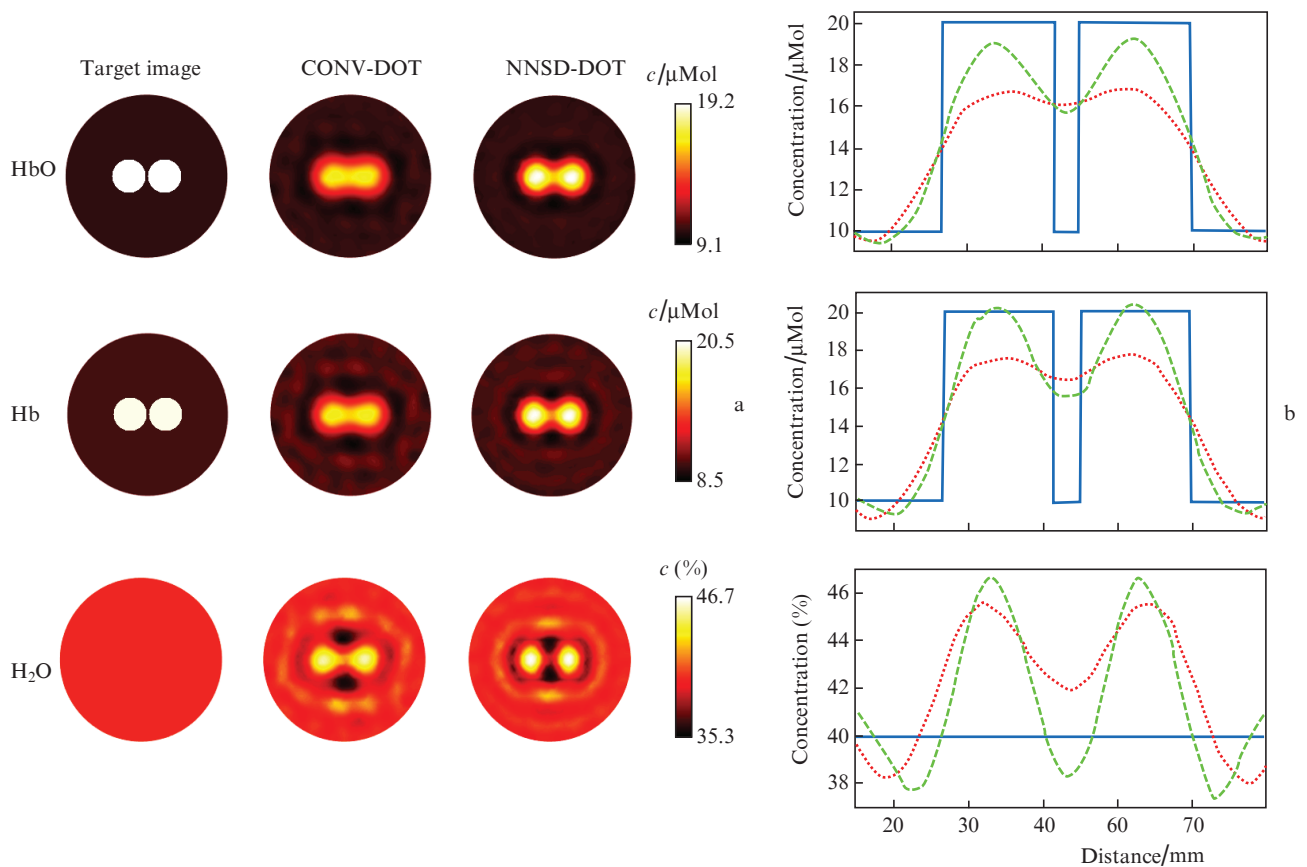
Figure 5. Example simulation with the tHb anomaly pair at 18 mm centroid separation (0.0278 cycles per mm) with (a) reconstructions for all three chromophores using either algorithm and (b) corresponding line profiles [(solid curves) for a target image; (dotted and dashed curves) for reconstructions obtained using CONV-DOT and NNSD-DOT, respectively] along central 56 mm of the horizontal diameter.

lies included, both with 2:1 contrast in Hb and HbO, and their respective centroids located on the model's horizontal diameter symmetrically about the model centre, as demonstrated in Fig. 5a. The modulation transfer coefficient (MTC) was used as a quantitative metric to assess the ability to resolve the two anomalies [23], defined as the relative percentage depth of the trough minimum compared to the mean of the two peaks in the horizontal diameter line profile. The anomalies radial distances were simultaneously altered to give centroid separation distances between 16 mm and 30 mm, in 2 mm intervals, evaluated for 10 repeats when either 0%, 0.5% or 1% Gaussian noise was added to the simulated data.

At 18 mm separation distance, distinguishing the anomaly pair was challenging with CONV in images of both Hb and HbO, whilst the distinct anomalies were clearly visible when using the NNSD algorithm in Fig. 5a, with more well-defined peaks in their corresponding line profiles for NNSD (Fig. 5b). This difference in resolution was also evident in cross-talk signals occurring in water images. The consistently higher MTC values seen with NNSD quantitatively support this observation in Fig. 6, particularly at shorter separations corresponding to around 0.02 to 0.03 cycles per mm; however, as the added noise was increased any comparative improvements attained from NNSD over CONV became less significant.

4. Spatial derivative sensitivity profile

To investigate the underlying mechanisms of the proposed algorithm, example sensitivity profiles of the Jacobian, either for NNSD or CONV, for a single source with index 1 and detectors with indices 9 and 10 on the opposing side, are shown in Fig. 7, with a clear distinction seen between the two algorithms. The two Jacobian profiles for neighbouring source-sharing source–detector pairs in Fig. 7a are indicative of the presence of some mutual information between their respective boundary data, in which any changes in underlying optical properties in the regions of overlap will contribute to both measurements.

In the spatial derivative approach, when subtracting nearest neighbour measurements, the sensitivity in these overlapping regions is diminished to some degree, resulting in

a reduced FWHM of the two peaks for the NNSD sensitivity plot compared to the single peak for the CONV sensitivity plot. Analysis of the singular values of J has previously been shown to be a useful approach for optimisation of density and field of view of optode arrangements [24]. To investigate the differences in the sensitivity profiles of the two algorithms further, singular value decomposition (SVD) of the respective Jacobian matrices results in a triplet of matrices, $J = USV^T$, where U and V are the matrices containing the corresponding singular orthonormal vectors of J, corresponding to the detection-space modes and image-space modes, respectively; and S is a diagonal matrix containing the singular values of J ordered in decreasing magnitude. The magnitude of these singular values indicates the relative contributions of these image-space modes on the detected signal and therefore the number of useful measurements above the data noise floor or modelling error.

Figure 8 reveals the NNSD algorithm provides higher singular value intensities for the same index. When considering a value of 1% for the noise and regularisation threshold, the number of singular values above this limit was 121 for CONV-DOT and 167 for NNSD-DOT. This increased number of singular values indicates that more useful measurements are contributing to the parameter recovery using the proposed NNSD algorithm.

## 5. Blood phantom. Experimental methods and results

Experimental data were used from imaging a blood-based gelatin cylindrical phantom with a diameter of 86 mm and height of 85 mm using a circular geometry CW spectrometer tomography system with a Ti:sapphire laser source [25]. A homogeneous phantom with background concentrations of approximately 85%, 11 µMol and 50% for StO_2, tHb and H_2O, respectively, was imaged and used to calibrate for the source and detector coupling and data/model mismatch, in addition to calculating a homogeneous fit used as an initial guess following a protocol presented previously [16]. A heterogeneous phantom was also imaged with intralipid solution added to a 25 mm diameter cylindrical hole containing concentrations of approximately 27 µMol tHb and about 95% water. Measurement data at 13 wavelengths (700, 720, 740, 750, 765, 780, 790, 800, 820, 840, 860, 880 and 900 nm) were
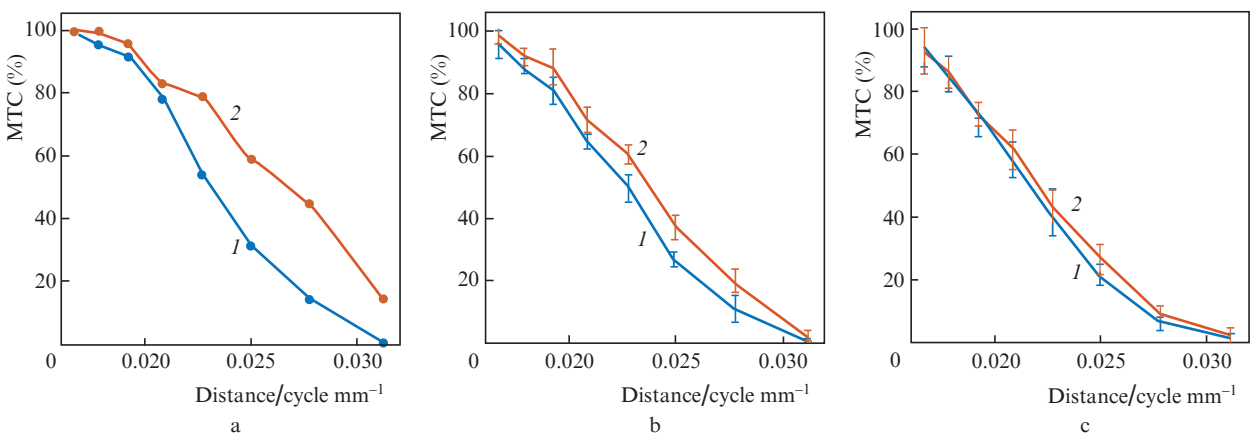
Figure 6. Variation in MTC for different cycles per mm of anomaly pair separation in Hb images, evaluated for both algorithms with (a) 0%, (b) 0.5% or (c) 1% Gaussian noise added to the boundary data for either (*1*) CONV-DOT or (*2*) NNSD-DOT.
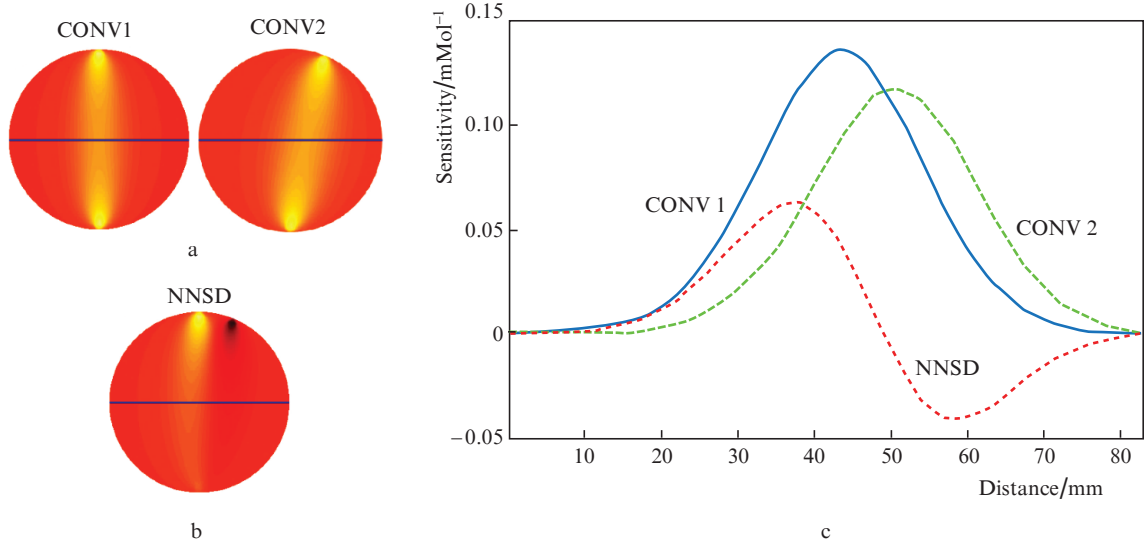
Figure 7. Plots of sensitivity for (a) the CONV Jacobian for two adjacent single source detector pair and (b) the resulting NNSD Jacobian for the subtraction of the two single source-sharing nearest neighbour pair of measurements, as well as (c) corresponding line profiles along the horizontal diameter of all three sensitivity profiles.
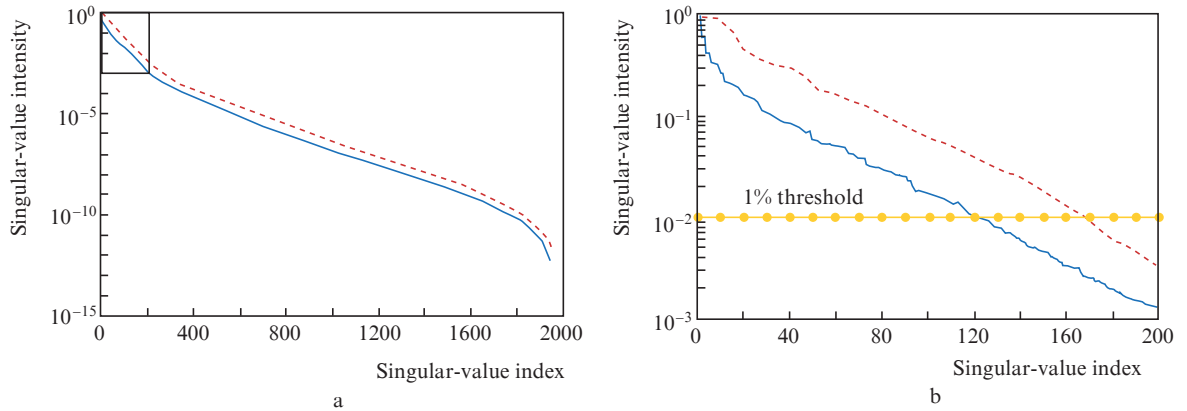
Figure 8. Normalised singular value plots for both (solid curve) CONV-Jacobian and (dashed curve) NNSD-Jacobian and (b) a zoomed version of region highlighted in the box.

used for the reconstruction and the FEM mesh used was identical to simulations in Fig. 1.

A qualitative improvement in contrast of the anomaly is evident using the NNSD-based algorithm for reconstructed 2D images of tHb and H_2O in Fig. 9, with improved resolution of the anomaly and greater contrast observed, which can be more clearly visualised in the corresponding line profiles running through the anomaly centre. Compared to CONV-DOT, artefacts at the boundary close to the anomaly were less significant, but the background appears less homogeneous with more image artefacts at depth for the NNSD-based algorithm, consistent with the amplification of Gaussian noise observed in simulation. All three quantitative evaluation metrics were calculated for the recovered images

Table 3. Quantitative evaluation metrics for reconstructed images from experimental gelatin phantom data, recovered using the NNSD-DOT and CONV-DOT algorithms.

Parameter	tHb		StO$_2$		H$_2$O	
	NNSD-DOT	CONV-DOT	NNSD-DOT	CONV-DOT	NNSD-DOT	CONV-DOT
Ground truth RC	2.17	–	–	–	1.9	–
RC	2.45	1.67	–	–	1.62	1.58
MSE	3.2×10^{-3}	2.1×10^{-3}	9.4×10^{-6}	1.1×10^{-5}	1.3×10^{-2}	7.8×10^{-3}
AR	0.37	0.66	–	–	0.40	0.79
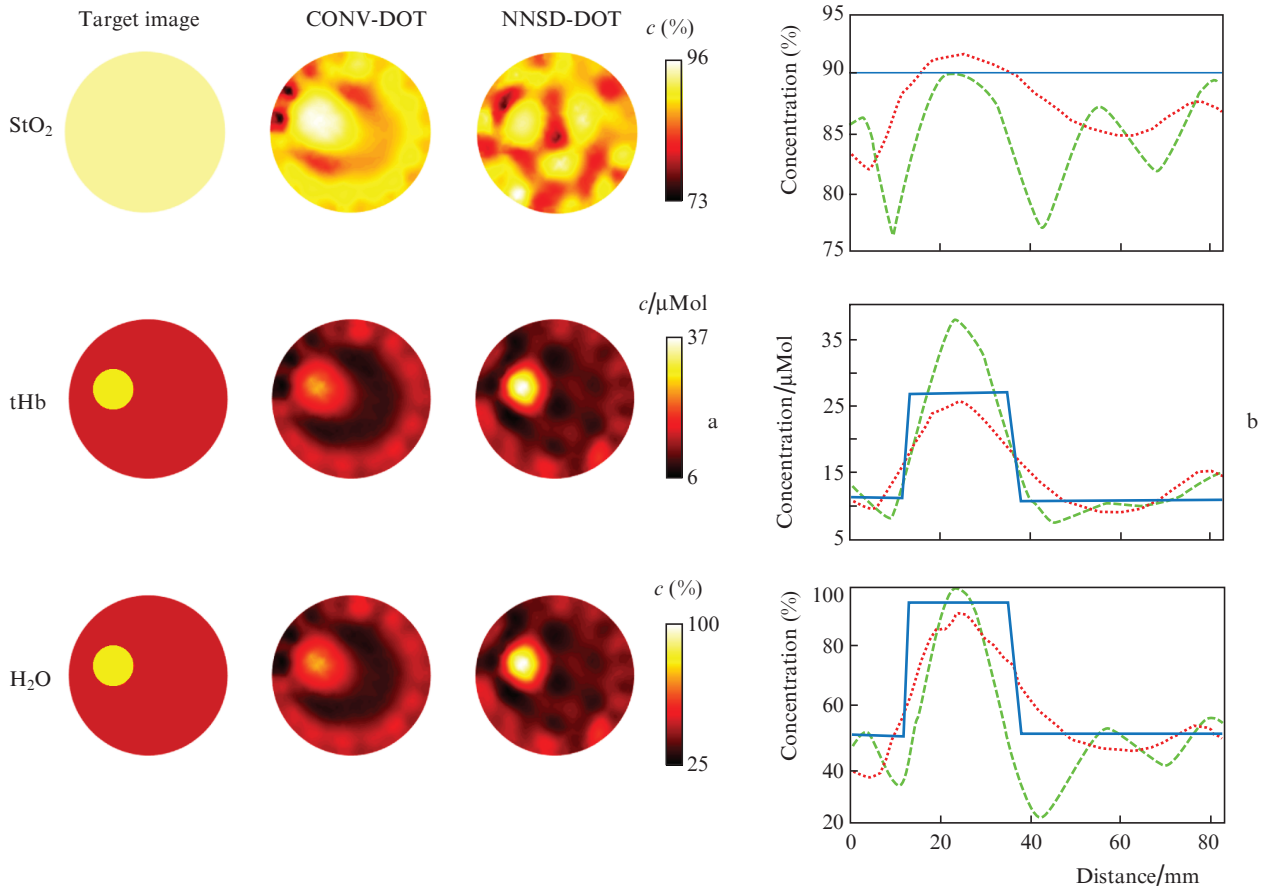
Figure 9. (a) Reconstructed tHb and H_2O anomaly for a gelatin based phantom, using both algorithms and (b) line profiles running along the diameter through both the centre of the anomaly and the centre of the mesh for (solid curve) a target image and reconstructions obtained using (dotted curve) CONV-DOT and (dashed curve) NNSD-DOT.

and support the same conclusions, with higher RC values and lower AR for both tHb and H_2O, whilst MSE values were greater for both these variables, as in Table 3.

6. Discussion and conclusions

The dominance of scattering over absorption in diffuse transport results in the commonly described 'banana shape' sensitivity distribution between a single source and detector pair, as shown in Fig. 5 and consequently resolution in recovered DOT images typically deteriorates with increased depth due to the widening of this sensitivity profile. In this work, an algorithm has been presented, based on the spatial derivative of the nearest neighbour detector pairs, and its performance is evaluated and compared to conventional reconstruction for inward-facing circular geometries. Using this NNSD-DOT algorithm, results from simulations in the absence of noise demonstrated a consistent improvement in both quantitative accuracy and resolution of recovered anomalies at depth, for regions towards the centre of the circle. Distinctive Jacobian plots were seen between the NNSD and CONV algorithms, with the former containing regions of both positive and negative values. Although it is impossible to increase the total information content in the boundary data without taking additional measurements, by subtracting neighbouring measurements in this way for NNSD, some mutual information from the overlapping regions of the individual sensitivity profiles for these two neighbouring measurements will be

cancelled and therefore eliminated from the update at that iteration. It is hypothesised that the resulting narrower FWHM of the Jacobian observed for NNSD compared to CONV causes an increase in number of useful singular values and hence more useful orthonormal components during fitting, as compared to CONV-DOT. This allows the NNSD approach to achieve the demonstrated improvements in resolution and depth sensitivity without the need for additional measurements or the introduction of spatially variant regularisation [26] or depth compensation algorithms [27], which by altering the model can potentially introduce additional artefacts.

In the presence of 0.5% and 1% noise during simulated studies, the performance of NNSD algorithm was more complex, with significant improvements seen at certain depths and for certain chromophores, although increases in total MSE were observed across the whole image in certain cases. Recovered images using experimental data acquired for a gelatin phantom containing an anomaly, also supported the same conclusions, with improvement in contrast and resolution of the anomaly using NNSD, but greater MSE. Whenever two or more measurements are combined to produce a new data set, such as in difference imaging, spectral derivative or spatial derivative algorithms, Gaussian noise will inherently be amplified. For example, in CW imaging, a 1% intensity noise in CONV-DOT is equivalent to 1.41% noise when two intensity measurements are combined. Evidence of this noise amplification can be seen in previously published work, with

significant boundary artefacts clearly visible, both for simulations with noise and experimental data when using the geometric-sensitivity-difference based algorithm [13]. In cases of high noise, it could therefore be argued that the NNSD-DOT algorithm may not be beneficial, however by implementing approaches for reducing Gaussian noise NNSD-DOT may still prove useful, such as taking the average of multiple repeat measurements or if the given imaging setup allows for derivative based calibration free imaging, such as has been proposed previously [12], the resulting noise will be the same as in calibrated CONV-DOT.

Improvements in quantitative accuracy are useful in clinical applications for the diagnosis of disease, such as detecting breast cancer or arthritis in the joint. Simulations using a simple heterogeneous breast model demonstrated a potential $15\%-25\%$ improvement in quantitative accuracy of recovered physiological values by using the proposed NNSD-DOT algorithm. Circular inwards-facing optode geometries are a unique case for tomography, in which a combination of both reflectance and transmission measurements are acquired with rotational symmetry. Any improvements in information content and consequently resolution resulting from the NNSD measurements will therefore also be observed in all directions. Although enhancements have been demonstrated for this specific circular imaging setup, this result cannot be generalised to other imaging geometries as any enhancement will be both geometry specific and dependent on source and detector locations. Application of the NNSD algorithm for recovery of abnormalities in both scattering and absorption with frequency domain data, or in cases with non-broadband data at only two wavelengths to recover only two abnormalities in HbO and Hb, were also investigated in simulation experiments. The results of these studies were not included in the main text due to space considerations but revealed similar conclusions. In addition, an equivalent 3D cylindrical model with the same source–detector set-up located on the circular boundary of a 2D cross-sectional plane was similarly found to provide superior resolution and contrast with NNSD, however further characterisation is required to assess the impact of more complex source–detector configurations, such as the inclusion of combinations not lying within the same 2D cross-sectional plane.

In conclusion, this work has demonstrated the potential enhancements in resolution and contrast achievable by using a nearest neighbour, spatial derivative DOT algorithm to recover absolute chromophore distributions for inwards-facing circular imaging geometries, such as those used to monitor diseases of the breast or joint. An associated increase in the intensity of singular values of the Jacobian matrix compared to conventional DOT has provided insight into the mechanisms behind spatial-differential methods. Future work is required to systematically explore the parameter estimation and other weighted combinations of source–detector pairs, in order to optimize and generalize this algorithm to a wider variety of imaging configurations.

References

1. Arridge S.R., Schweiger M. *Opt. Express*, **2**, 213 (1998).
2. Hielscher A.H., Klose A.D., Hanson K.M. *IEEE Trans. Med. Imaging*, **18**, 262 (1999).
3. Jiang H., Paulsen K.D., Osterberg U.L., et al. *J. Opt. Soc. Am. A*, **13**, 253 (1996).
4. Dehghani H., Eames M.E., Yalavarthy P.K., et al. *Int. J. Numer. Methods Biomed. Eng.*, **25**, 711 (2009).
5. Xu H., Pogue B.W., Springett R., et al. *Opt. Lett.*, **30**, 2912 (2005).
6. Dehghani H., Leblond F., Pogue B.W., et al. *Phys. Med. Biol.*, **55**, 3381 (2010).
7. Wang J., Pogue B.W., Jiang S., et al. *Proc. SPIE*, **7174**, 71740H (2009).
8. Suzuki S., Takasaki S., Ozaki T., et al. *Proc. SPIE*, **3597**, 582 (1999).
9. Gunadi S., Leung T.S., Elwell C.E., et al. *Biomed. Opt. Express*, **5**, 2896 (2014).
10. Milej D., Abdalmalak A., McLachlan P., et al. *Biomed. Opt. Express*, **7**, 4514 (2016).
11. Eggebrecht A.T., Ferradal S.L., Robichaux-Viehoever A., et al. *Nat. Photonics*, **8**, 448 (2014).
12. Naser M.A., Patterson M.S., Wong J.W. *Biomed. Opt. Express*, **3**, 2794 (2012).
13. Xu G., Piao D. *Med. Phys.*, **40**, 013101 (2013).
14. McBride T.O., Pogue B.W., Jiang S. *Rev. Sci. Instrum.*, **72**, 1817 (2001).
15. Yuan Z., Zhang Q., Sobel E., et al. *J. Biomed. Opt.*, **12**, 034001 (2007).
16. Dehghani H., Pogue B.W., Poplack S.P., et al. *Appl. Opt.*, **42**, 135 (2003).
17. Tikhonov A.N. *Dokl. Akad. Nauk SSSR*, **151**, 501 (1963).
18. Corlu A., Choe R., Durduran T., et al. *Appl. Opt.*, **44**, 2082 (2005).
19. Srinivasan S., Pogue B.W., Jiang S., et al. *Appl. Opt.*, **44**, 1858 (2005).
20. van Staveren H., Moes C., van Marle J., Prahl S., van Gemert M. *Appl. Opt.*, **30**, 4507 (1991).
21. Brooksby B., Srinivasan S., Jiang S., et al. *Opt. Lett.*, **30**, 1968 (2005).
22. Srinivasan S., Pogue B.W., Jiang S., et al. *PNAS*, **100**, 12349 (2003).
23. Lyubimov V.V., Kalintsev A.G., Konovalov A.B., et al. *Phys. Med. Biol.*, **47**, 2109 (2002).
24. Culver J., Ntziachristos V., Holboke M., et al. *Opt. Lett.*, **26**, 701 (2001).
25. Wang J., Jiang S., Li Z., et al. *Med. Phys.*, **37**, 3715 (2010).
26. Pogue B.W., McBride T.O., Prewitt J., et al. *Opt. Lett.*, **38**, 2950 (1999).
27. Niu H., Tian F., Lin Z.J., et al. *Opt. Lett.*, **35**, 429 (2010).